RESEARCH ARTICLE SUMMARY

NEUROSCIENCE

Compartment-specific tuning of dendritic feature selectivity by intracellular Ca^{2+} release

Justin K. O'Hare, Kevin C. Gonzalez†, Stephanie A. Herrlinger†, Yusuke Hirabayashi†, Victoria L. Hewitt, Heike Blockus, Miklos Szoboszlay, Sebi V. Rolotti, Tristan C. Geiller, Adrian Negrean, Vikas Chelur, Franck Polleux*‡, Attila Losonczy*‡

INTRODUCTION: Synaptic plasticity, the process by which neurons adjust the strengths of their thousands of inputs, allows animals to adapt to their environment. Decades of research have established Ca^{2+} as a central mediator of synaptic plasticity. Historically, most investigations into the role of Ca^{2+} in plasticity have focused on its influx through voltage-gated channels that open when synaptic input depolarizes a neuron. However, a large body of in vitro research suggests that an alternate source of Ca^{2+} may also play a potent role in shaping plasticity: the endoplasmic reticulum (ER). The ER stores Ca^{2+} in vast quantities within a cell and can release this store in response to strong synaptic input through intracellular Ca^{2+} release (ICR). The ER is therefore poised to shape the magnitude and spatial distribution of Ca^{2+} during plasticity induction. Despite its potential role in synaptic plasticity, ICR has never been investigated in mammalian neurons in vivo.

RATIONALE: To test whether ICR participates in experience-dependent plasticity, we focused on pyramidal neurons of hippocampal area CA1 (CA1PNs). CA1PNs receive excitatory inputs from multiple afferent circuits, carrying complementary streams of information about an animal's environment that impinge onto distinct compartments of the CA1PN dendritic arbor. As an animal explores a new environment, CA1PNs integrate these inputs to form spatially tuned receptive fields known as place fields that manifest as a neuron firing when an animal occupies a particular location. Recent work has characterized an in vivo plasticity mechanism driving place field formation: behavioral time-scale plasticity (BTSP). BTSP is initiated by a large, prolonged dendritic depolarization (plateau potential) that ultimately potentiates synaptic inputs received during a seconds-long time window corresponding to the time of plateau onset.

Here, we used CA1PNs and BTSP as a model system to test whether ICR participates in the experience-dependent emergence of feature selectivity. We implemented a series of tools based on single-cell electroporation allowing us to (i) manipulate the cytosolic impact of ICR at single-cell resolution using conditional gene deletion, (ii) optogenetically induce place cells, and (iii) image somatic and dendritic Ca^{2+} dynamics simultaneously during spatial navigation.

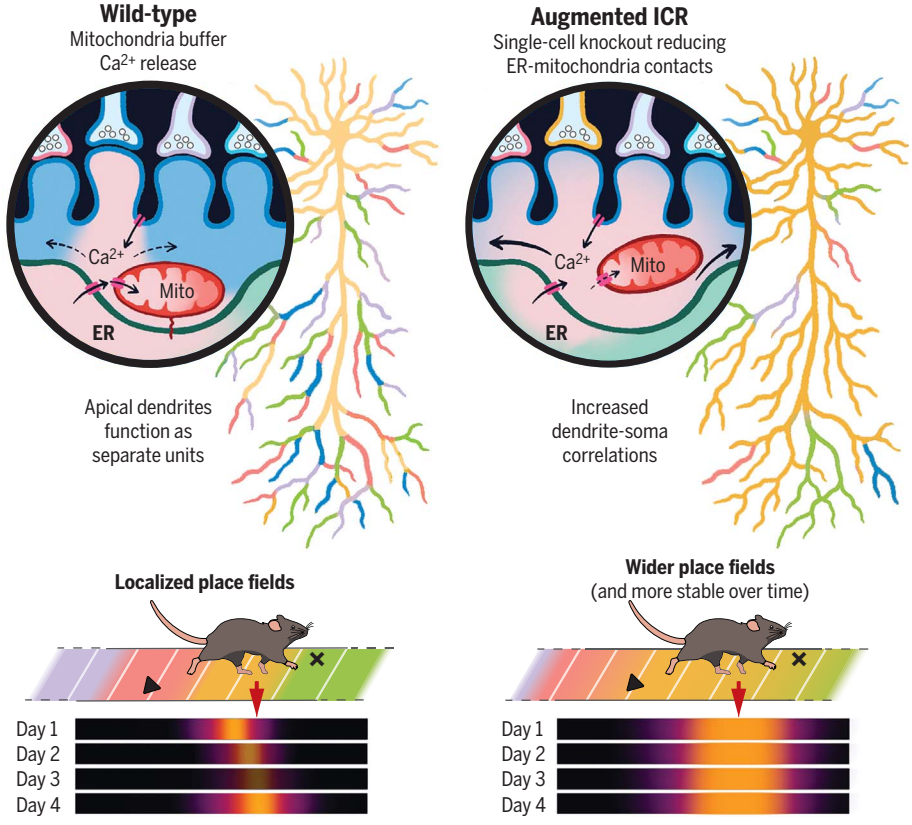

ICR shapes receptive fields important for spatial navigation. We tested the role of ICR in neuronal feature selectivity by genetically ablating contact sites between ER and mitochondria (Mito) in single pyramidal neurons of hippocampal area CA1 in vivo. Increasing the impact of ICR on cytoplasmic Ca^{2+} altered integrative properties in apical dendrites, widening and stabilizing "place fields" over time.

ILLUSTRATION BY MATTEO FARINELLA

RESULTS: The gene *Pdzd8* encodes a recently identified ER-mitochondrial tethering protein that, when deleted, leads to unrestricted ICR. We found that *Pdzd8* deletion in single adult CA1PNs in vivo substantially increased the level of spatial co-tuning observed in their apical dendrites relative to the soma of CA1 place cells, a phenomenon not observed in basal dendrites, which were already highly co-tuned with the soma in control CA1PNs. Maximizing ICR leads to more-stable retention of place cell spatial tuning over time and alters the integrative properties of their apical dendrites to shape output-level receptive fields.

CONCLUSION: ICR plays a key and previously uncharacterized role in shaping the dendritic integration properties of CA1PNs during the emergence of feature selectivity. Therefore, ICR cooperates with circuit-level architecture in vivo to promote the emergence of behaviorally relevant forms of plasticity in a compartment-specific manner. ■

The list of author affiliations is available in the full article online.
***Corresponding author. Email: al2856@columbia.edu (A.L.); fp2304@columbia.edu (F.P.)**
†These authors contributed equally to this work.
‡These authors contributed equally to this work and are co-senior authors.
Cite this article as J. K. O'Hare *et al.*, *Science* 375, eabm1670 (2022). DOI: 10.1126/science.abm1670

READ THE FULL ARTICLE AT
https://doi.org/10.1126/science.abm1670

RESEARCH ARTICLE

NEUROSCIENCE

Compartment-specific tuning of dendritic feature selectivity by intracellular Ca^{2+} release

Justin K. O'Hare[1,2], Kevin C. Gonzalez[1,2]†, Stephanie A. Herrlinger[1,2]†, Yusuke Hirabayashi[3]†, Victoria L. Hewitt[1,2], Heike Blockus[1,2], Miklos Szoboszlay[1,2], Sebi V. Rolotti[1,2], Tristan C. Geiller[1,2], Adrian Negrean[1,2], Vikas Chelur[1], Franck Polleux[1,2,4]*‡, Attila Losonczy[1,2,4]*‡

Dendritic calcium signaling is central to neural plasticity mechanisms that allow animals to adapt to the environment. Intracellular calcium release (ICR) from the endoplasmic reticulum has long been thought to shape these mechanisms. However, ICR has not been investigated in mammalian neurons in vivo. We combined electroporation of single CA1 pyramidal neurons, simultaneous imaging of dendritic and somatic activity during spatial navigation, optogenetic place field induction, and acute genetic augmentation of ICR cytosolic impact to reveal that ICR supports the establishment of dendritic feature selectivity and shapes integrative properties determining output-level receptive fields. This role for ICR was more prominent in apical than in basal dendrites. Thus, ICR cooperates with circuit-level architecture in vivo to promote the emergence of behaviorally relevant plasticity in a compartment-specific manner.

Learning occurs when experience-driven neuronal activity patterns induce changes in synaptic strengths, thereby altering how future information propagates through neuronal circuits. This process, known as synaptic plasticity, is a fundamental way in which animals adapt to the environment and yet it remains enigmatic. At the cellular level, Ca^{2+} helps to transduce specific patterns of synaptic activation into long-lasting changes in synaptic efficacy (*1*). The magnitude and spatiotemporal patterning of cytosolic Ca^{2+} are therefore critical in determining which synapses will undergo plasticity and the extent to which they will do so. Most studies of the mechanisms regulating dendritic Ca^{2+} dynamics have focused on the role of voltage-gated channels mediating Ca^{2+} conductances at the plasma membrane (*2*–*4*). However, another regulator of intracellular Ca^{2+} dynamics is the main internal Ca^{2+} store, the endoplasmic reticulum (ER) (*5*), which pervades the dendritic arbor (*6*–*8*), where it sequesters nearly all Ca^{2+} within a neuron. The ER can release its highly concentrated store of Ca^{2+} in an activity-dependent manner, significantly amplifying the impact of Ca^{2+} influx from the extracellular space (*5*, *9*–*14*).

Although much attention has been paid to the potential role for intracellular Ca^{2+} release (ICR) in plasticity in numerous in vitro studies (*11*–*21*), and recently in *Drosophila* (*22*), this powerful intracellular amplificatory process remains unexplored in mammalian neurons in vivo because of the lack of tools to precisely and effectively manipulate ICR in awake, behaving vertebrates. Such an approach would require not only cellular and pre- versus postsynaptic specificity but also the ability to influence ICR across each of its two canonical release mechanisms (*5*, *23*). To overcome this limitation, we focused on *Pdzd8*, a gene that encodes a tethering protein that brings ER and mitochondria into direct contact, thereby enabling mitochondria to buffer a substantial fraction of ER-released Ca^{2+} (*9*). Reduction of *Pdzd8* expression allows ~50% more Ca^{2+} to escape into the cytosol upon synaptically driven ICR in dendrites while leaving functional and morphological properties of the ER and mitochondria intact (*9*). Therefore, *Pdzd8*-mediated ER-mitochondria contacts present an avenue to manipulate ICR in vivo across its multiple release pathways.

Here, we leveraged *Pdzd8* deletion as a gain-of-function tool to augment the cytosolic impact of ICR. We deployed this molecular-genetic tool in pyramidal neurons of hippocampal area CA1 (CA1PNs). The CA1PN is a rich model system with which to investigate the general principles of experience-dependent synaptic plasticity. It receives diverse, circuit-specific excitatory inputs transmitting complementary streams of information relevant to an animal's environment, and these inputs target dendritic compartments that are morphologically and biophysically distinct from one another (*24*–*29*). As an animal explores its environment, CA1PNs integrate these diverse inputs to generate spatially tuned receptive fields, known as "place fields" (PFs), which manifest as the cell selectively firing when the animal occupies a particular location within the environment and collectively form a comprehensive map of an animal's environment (*30*, *31*). Recent work has established a plasticity mechanism, known as behavioral time-scale plasticity (BTSP) (*32*–*34*), which is sufficient to drive rapid PF formation in CA1PNs. BTSP is driven by large, prolonged dendritic depolarization events, known as plateau potentials, which potentiate dendritic spines receiving presynaptic input within a seconds-long temporal window surrounding plateau potential onset. We leveraged the well-characterized functional-anatomical complexity of CA1PNs and the robust in vivo plasticity mechanism BTSP to test the role of ICR in synaptic plasticity mechanisms supporting dendritic and cellular feature selectivity.

Single-cell genetic deletion and in vivo subcellular imaging in hippocampal area CA1

We simultaneously monitored the activity of dendrites and their cognate somata in CA1PNs with either normal or augmented ICR during spatial navigation. Using in vivo single-cell electroporation (see the materials and methods), we introduced pCAG-Cre, pCAG-FLEX-jGCaMP7b, and pCaMKII-bReaChes-mRuby3 to single CA1PNs in anesthetized adult mice (Fig. 1A, left and middle). We targeted single cells in a *Pdzd8* conditional knockout mouse line $Pdzd8^{F/F}$ (fig. S1, A and B) and in wild-type (WT) control mice to generate single *Pdzd8*-knockout (KO) (augmented ICR) and WT cells (Fig. 1A, right) expressing a high-baseline

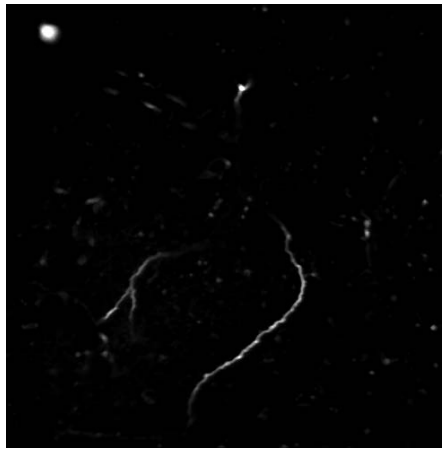

Movie 1. Somatic (left) and apical dendritic (right) imaging planes of example CA1PN shown in Fig. 1B (right) displayed side by side during a PF induction lap. jGCaMP7b response to a single, 1-s LED pulse is shown. Frames are motion corrected and shown at actual speed. Data were acquired using two-photon microscopy with a 40× objective lens at 1.0× optical zoom.

[1]Department of Neuroscience, Columbia University, New York, NY 10027, USA. [2]Mortimer B. Zuckerman Mind Brain Behavior Institute, Columbia University, New York, NY 10027, USA. [3]Department of Chemistry and Biotechnology, School of Engineering, The University of Tokyo, Tokyo 113-8656, Japan. [4]Kavli Institute for Brain Science, Columbia University, New York, NY 10027, USA.
*Corresponding author. Email: al2856@columbia.edu (A.L.); fp2304@columbia.edu (F.P.)
†These authors contributed equally to this work. ‡These authors contributed equally to this work and are co-senior authors.

Ca^{2+} indicator (jGCaMP7b) and a fluorescently tagged excitatory opsin (bReaChes-mRuby3). In vivo single-cell electroporation of a Cre-expressing plasmid in *Pdzd8*$^{F/F}$ mice eliminated *Pdzd8* mRNA within 3 days (fig. S1, C to F) and expression of Cre recombinase in cortical neurons reduced PDZD8 protein levels within 7 days (fig. S1, G and H). We performed all imaging experiments no less than 7 days after electroporation. Our acute, single-cell genetic deletion in adult CA1PNs circumvented potential non–cell-autonomous (*22*, *35*) and developmental (*16*) effects that might have arisen from broad and constitutive perturbations. During head-fixed spatial navigation on a cue-rich, 2-m treadmill belt (*36*, *37*), we simultaneously monitored activity dynamics in one dendritic focal plane, which ranged from basal dendrites in stratum oriens to distal tuft dendrites in stratum lacunosum moleculare (fig. S2), and in a somatic plane that often contained coplanar segments of basal dendrite (Fig. 1, B and C, and Movie 1). For motion correction (fig. S3) and dendritic

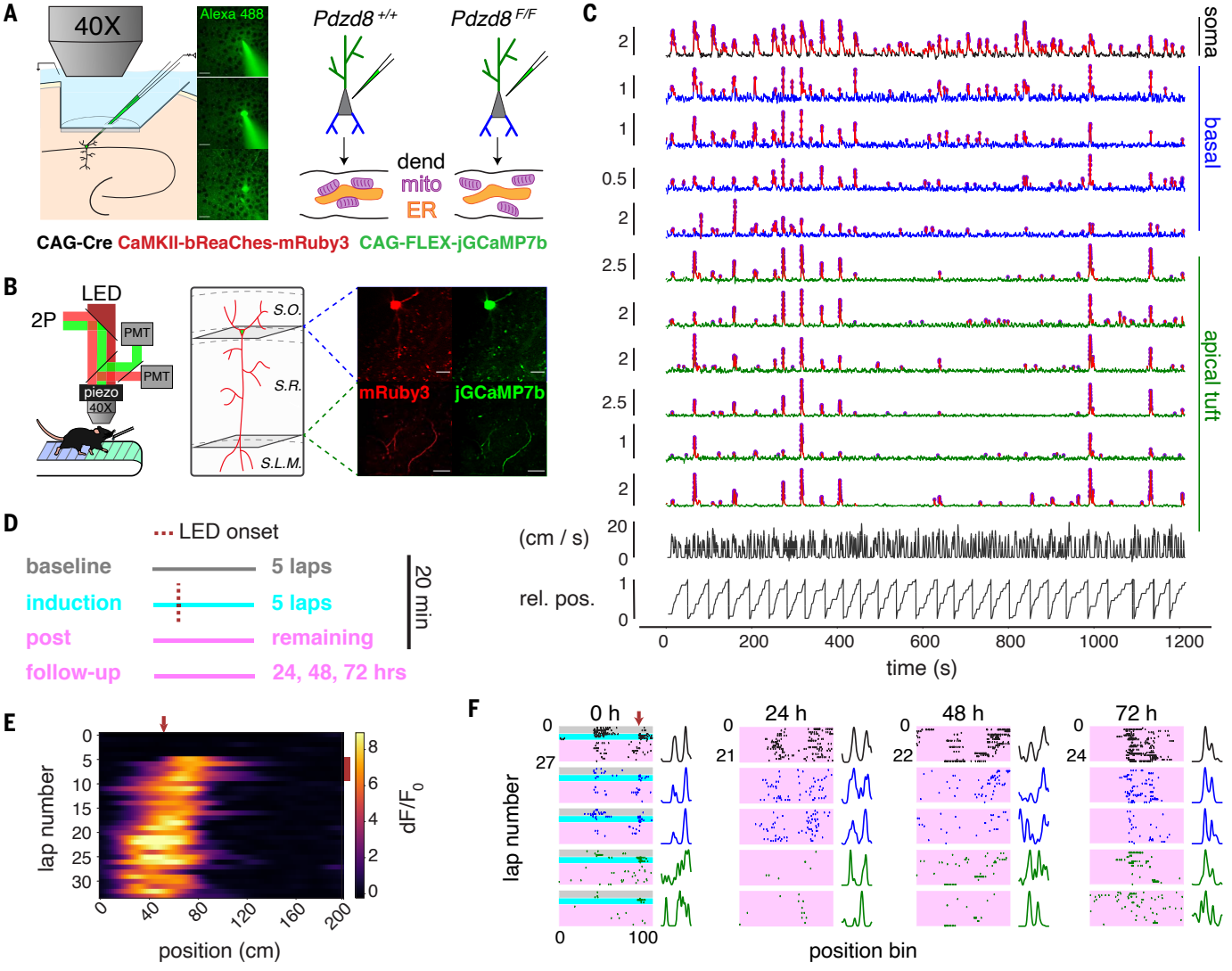

Fig. 1. Simultaneous imaging of somatic and dendritic activity in single, spatially tuned CA1PNs with normal and augmented ICR. (**A**) Left: An electroporation pipette containing plasmid DNAs (listed below) is guided through a silicon-protected slit in an imaging window implanted over dorsal CA1. Middle: Two-photon images before (top), during (middle), and after (bottom) electroporation of plasmid solution to a single cell in the pyramidal layer. Scale bar, 20 μm. Right: Plasmid mixture is delivered through single-cell electroporation to CA1PNs in *Pdzd8*$^{+/+}$ and *Pdzd8*$^{F/F}$ mice. Schematic shows Cre-mediated ablation of ER-mitochondria (mito) contacts in dendrite (dend) of *Pdzd8*$^{F/F}$ CA1PN, augmenting cytosolic impact of ICR. (**B**) Left: Multiplane, dual-channel imaging during head-fixed spatial navigation. LED (620 nm) was used for photoactivation of the opsin-expressing cell. Right: Diagram approximating focal planes imaged for an example cell with corresponding motion-corrected, time-averaged fields of view from each channel showing soma/coplanar basal dendrites (top row) and distal apical tuft dendrites (bottom row). Scale bar, 50 μm. Hippocampal strata are indicated by dashed lines. S.O., stratum oriens; S.R., stratum radiatum; S.L.M., stratum lacunosum moleculare. (**C**) Traces of soma (black), as well as basal (blue) and apical tuft (green) dendrites coacquired from example cell in (B). Vertical scale bars indicate dF/F_0. Detected Ca^{2+} transients are shown in red with deconvolved events as magenta circles. Frame-synchronized animal running speed and relative position (rel. pos.) are shown below traces. (**D**) Schematic describing optogenetic PF induction paradigm. (**E**) Somatic activity heatmap from induction session. LED location is denoted by the red arrow at top; LED laps by red bar at right. (**F**) Event rasters and spatial TCs from a single CA1PN showing somatic and subset of dendritic dynamics on induction day (0 hours) and at the 24-, 48-, and 72-hour time points. ROI types are colored as in (C); conditions are colored as in (D). TCs are scaled to maximum values to aid visualization.

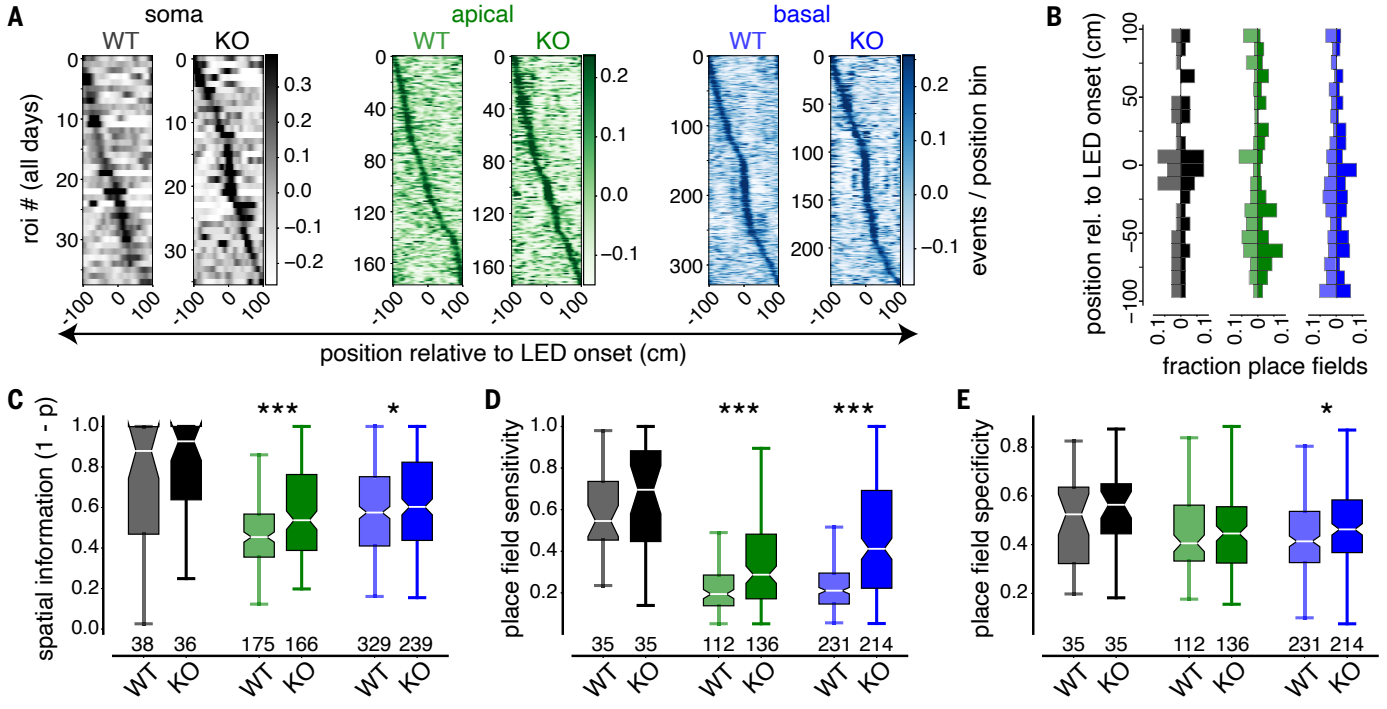

Fig. 2. Effect of augmented ICR on somatic and dendritic spatial tuning properties in single CA1PNs. (**A**) Spatial activity heatmaps showing LED-centered spatial TCs for all *Pdzd8* KO and WT somatic (greys), apical (greens), and basal (blues) ROIs imaged across all days, sorted by TC peak location. (**B**) Mirrored vertical histograms showing distribution of PF center locations relative to LED onset for *Pdzd8* WT (transparent; left of *x*-axis) and KO (opaque; right of *x*-axis) for somatic, apical, and basal ROIs color coded as in (A). (**C** to **E**) PF metrics, including spatial information (C), PF sensitivity (D), and PF specificity (E), shown for all ROI type–genotype combinations. Boxes range from lower to upper quartiles with line at median; whiskers show range of data within 1.5 * (Q3 – Q1) of box boundaries. For (A) to (C), *N* represents the total number of ROIs imaged across days (see table S1 and and the supplementary materials and methods for details). For (D) and (E), *N* represents the total number of ROIs with significant spatial tuning across days. Two-sided unpaired *t* tests and Mann-Whitney *U* tests were used to determine statistical significance. $^{*}P < 0.05$; $^{***}P < 0.001$.

region of interest (ROI) registration (see the supplementary materials and methods), we coacquired static mRuby3 signals through a dedicated collection channel (Fig. 1B).

To evaluate the role of ICR in plasticity and learning, we sought to image CA1PNs expressing PFs. To boost the fraction (*36*, *38*) of CA1PNs functioning as "place cells" and to track the stability of a subset of PFs with a defined time zero, we performed an optogenetic PF induction protocol in each imaged cell (Fig. 1, D and E, and materials and methods). Optogenetically induced PFs displayed characteristic hallmarks (fig. S4, A to D) of naturally occurring in vivo place cell formation (*32*, *33*, *39*, *40*) and shared similar properties with spontaneous, noninduced PFs (fig. S4, E to G). We therefore pooled spontaneous and induced PFs except in longitudinal analyses addressing the stability of spatial feature selectivity, for which a defined time point for PF formation was necessary. We imaged somatic and dendritic activity in 20-min sessions on 4 consecutive days (Fig. 1F and fig. S5), including the initial PF induction day, comparing postinduction dynamics in CA1PNs with normal and augmented ICR.

Acute *Pdzd8* deletion as a tool to investigate the role of ICR

Given the absence of in vivo functional imaging data for apical CA1PN dendrites and the paucity of such data for basal dendrites (*41*–*43*), we first characterized spontaneous Ca^{2+} transient properties in apical and basal dendrites with respect to their parent soma and assessed any impact of our ICR-augmenting manipulation on basic CA1PN activity dynamics. *Pdzd8* KO and WT CA1PN cell bodies did not differ in Ca^{2+} transient frequency or amplitude (fig. S6, A and B). Isolated dendritic transients (no coincident somatic event; see fig. S6, C and D, for examples) were overall rare compared with somatic transients with minor but significant differences in event frequency between compartment and genotype (fig. S6E). Isolated apical dendritic Ca^{2+} transients, which have not previously been reported in CA1PNs, were larger and more frequent than those observed in basal dendrites (fig. S6, E and F). Increasing ICR through *Pdzd8* KO did not affect isolated transient amplitude in either dendritic compartment (fig. S6F). We cannot formally rule out the possibility that undetected somatic action potentials back-propagate into imaged dendrites and contribute to apparent isolated events. However, a difference in event amplitude between genotype would be reasonably expected if ICR were routinely activated in the setting of local dendritic Ca^{2+} transients.

To further assess the potential effects of acute *Pdzd8* KO on baseline Ca^{2+} handling and excitability in adult CA1PNs, we first compared isolated, single-spine Ca^{2+} transients (no coincident shaft-level event; see fig. S6, G and H, for examples) in a separate set of CA1PNs electroporated with pCAG-Cre, pCAG-NES-jRGECO1a, and pCAG-FLEX-eGFP. We imaged individual apical and basal dendritic segments at high magnification in $Pdzd8^{F/F}$ and WT control mice under light anesthesia on a treadmill belt lacking spatial cues (fig. S6, G and H, and supplementary materials and methods). Although isolated spine Ca^{2+} transients were generally of greater amplitude and frequency in apical versus basal dendrites, these event properties did not significantly differ between *Pdzd8* KO and WT CA1PNs (Fig. S6, I and J). Next, we compared the electrophysiological properties of *Pdzd8* KO and WT CA1PNs after targeting either AAV-CaMKII-Cre-mCherry or mCherry-only control virus to dorsal CA1 of

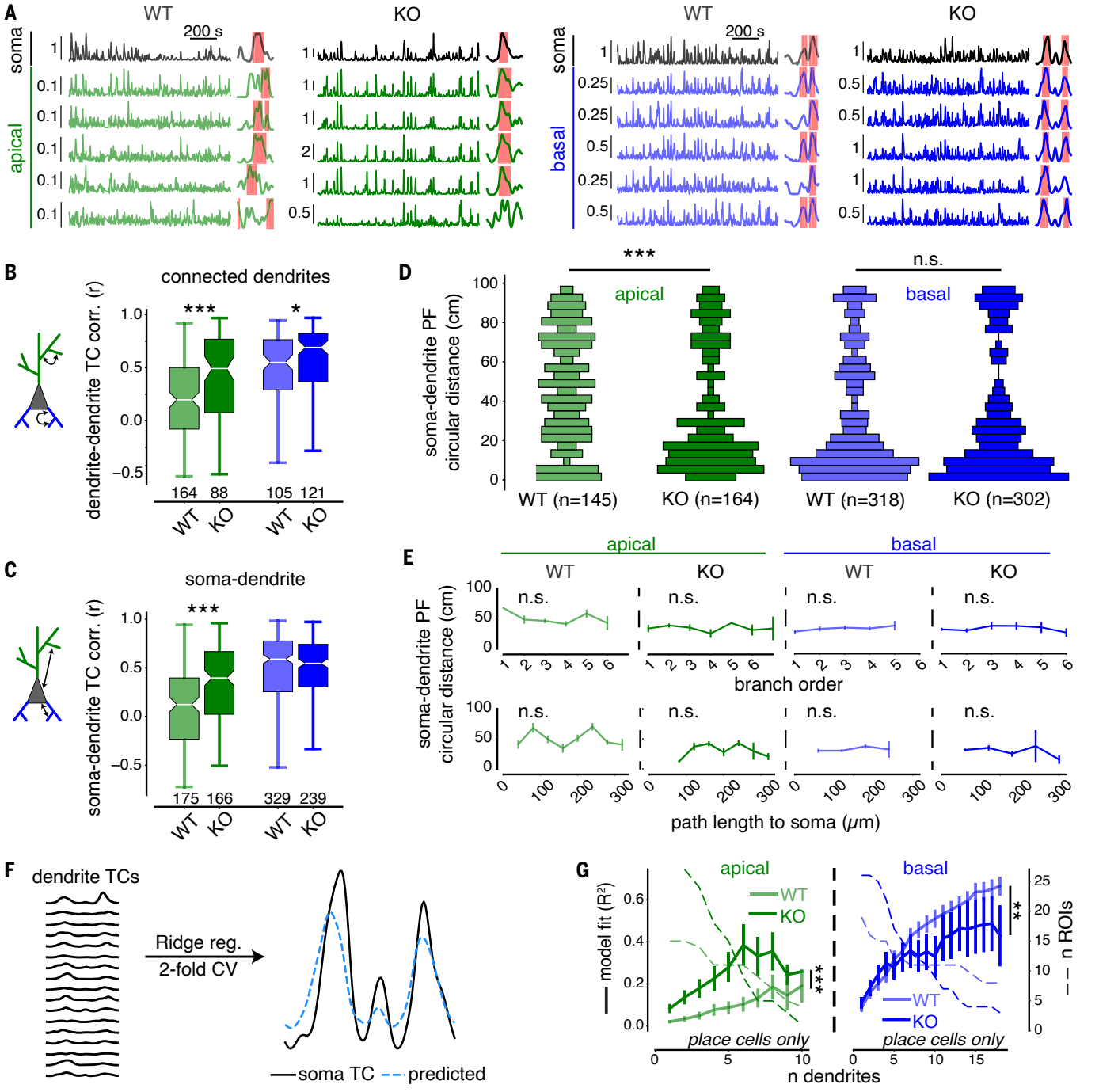

Fig. 3. Compartment-specific regulation of dendrite-dendrite and soma-dendrite co-tuning by ICR. (**A**) Example dF/F_0 traces and TCs for all ROI type-genotype combinations. Vertical scale bars indicate dF/F_0. Dendritic traces and TCs are grouped under corresponding somata. Detected PFs are denoted by pink shaded areas overlaid onto TCs. (**B** and **C**) TC correlations calculated exclusively between connected, co-imaged dendrites (B) (see fig. S8) and between dendritic ROIs and their corresponding somata (C). *N* represents the total number of ROIs imaged across days (table S1). Boxes range from lower to upper quartiles with line at median; whiskers show range of data within 1.5 * (Q3 − Q1) of box boundaries. (**D**) Vertical histograms showing distributions of minimum circular distances between somatic and dendritic PF centers. Bar widths represent relative abundance of bin values. *N* represents the total number of PFs from imaged dendrites belonging to place cells across days. (**E**) Circular distances in (D) plotted against branch order (top) and path length to soma binned every 40 μm (bottom). Pearson correlation analysis was used on nonbinned data. (**F**) Schematic for predicting somatic TC based on TCs of connected dendrites (see the supplementary materials and methods) with example performance shown at right. (**G**) Model performance (R^2) plotted against the number of dendrites included in training data. Number of cell sessions containing *N* dendrites is shown in dashed lines on the second *y*-axis. Note that measurement precision decreases with *N*. Apical two-way ANOVA, genotype effect: $F_{(1,43)} = 37.39$, $P < 0.001$); *n* dendrites effect: $F_{(9,217)} = 4.57$, $P < 0.001$; interaction: $F_{(9,217)} = 0.81$, $P > 0.05$; $n = 16$ WT and 28 KO place cells. Basal two-way ANOVA, genotype effect: $F_{(1,44)} = 7.35$, $P < 0.01$; *n* dendrites effect: $F_{(17,387)} = 13.44$, $P < 0.001$; interaction: $F_{(17,387)} = 1.05$, $P > 0.05$; $n = 19$ WT and 26 KO place cells. Error bars represent SEM. Distributions in (B) to (D) were compared using two-sided unpaired *t* tests and Mann-Whitney *U* tests. *$P < 0.05$, **$P < 0.01$, ***$P < 0.001$.

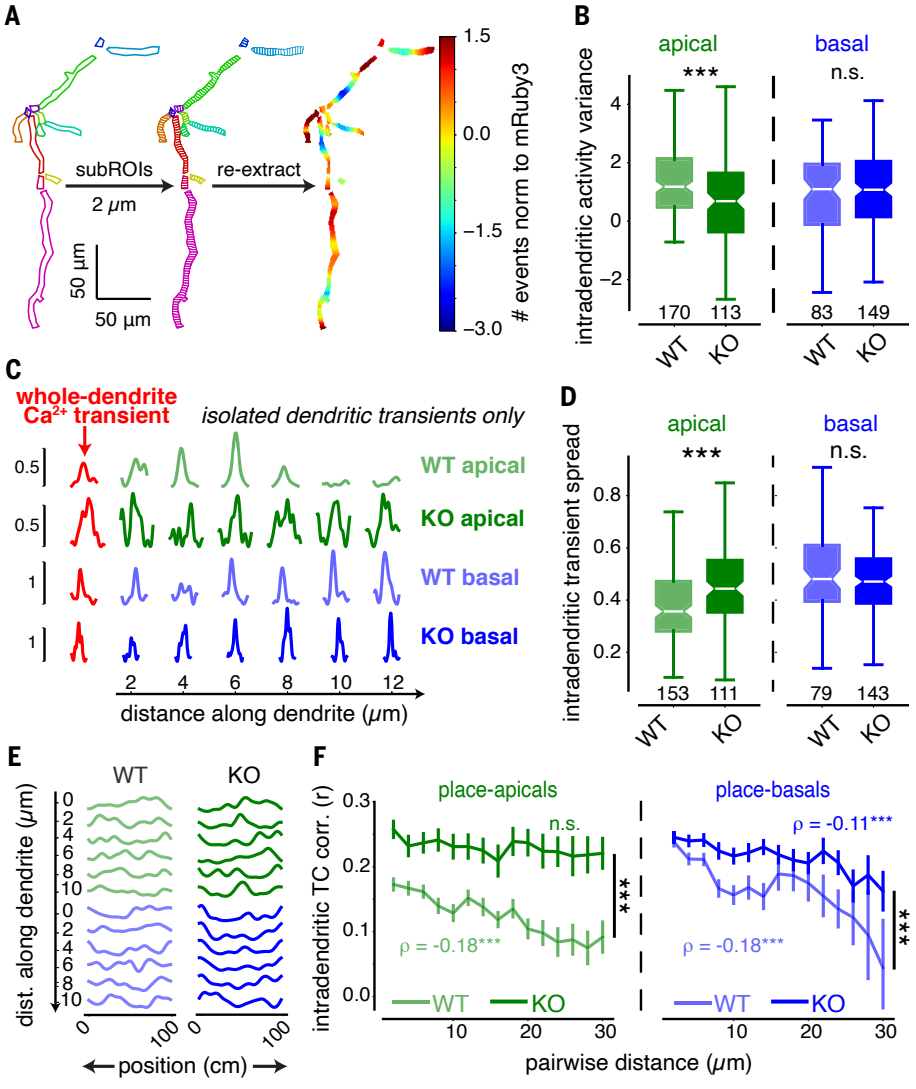

Fig. 4. Intracellular Ca^{2+} release shapes activity dynamics and spatial feature selectivity within single dendritic branches of CA1 PNs. (**A**) Approach to analyzing intradendritic dynamics. Each ROI was segmented into 2-μm sub-ROIs along its longest axis. Signals were then re-extracted from each sub-ROI for further analysis. Heatmap shows activity distribution for each imaged apical dendrite from a single WT CA1PN. Activity was normalized within ROIs to static mRuby3 signal intensity (log_2 ratio) to control for differences in focality (see the supplementary materials and methods). (**B**) Within-dendrite variance of activity levels between WT and *Pdzd8* KO apical and basal dendrites (log_2 ratio of coefficients of variation for events and mRuby3 signal intensity). (**C**) Spatial spread of isolated Ca^{2+} transients within single dendrites. For each Ca^{2+} transient detected from a whole-dendrite ROI (red traces), corresponding dF/F_0 signals are plotted from the first six sub-ROIs (12 μm) of that dendrite. (**D**) Normalized intradendritic spread of isolated Ca^{2+} transients within WT and *Pdzd8* KO apical and basal dendrites. A value of 1.0 indicates uniform sub-ROI peak amplitudes (see the supplementary materials and methods). (**E**) Sub-ROI spatial TCs, color coded as in (C). (**F**) Intradendritic TC correlations plotted as a function of distance separating two sub-ROIs (see the supplementary materials and methods). Spearman correlation coefficients are shown on plots. Distances were compared between genotypes using Mann-Whitney *U* tests. *N* = 110 WT and 100 KO place-apicals; 223 WT and 184 KO place-basals. Error bars represent SEM. Boxes range from lower to upper quartiles with line at median; whiskers show range of data within 1.5 * (Q3 − Q1) of box boundaries. Distributions in (B) and (D) were compared using two-sided unpaired *t* tests. ***$P < 0.001$.

adult $Pdzd8^{F/F}$ mice (fig. S7A and supplementary materials and methods). Apart from minor but significant differences in action potential amplitude and half-width, *Pdzd8* KO and WT CA1PNs shared similar electrophysiological attributes (fig. S7, B to K).

ICR controls the diversity and reliability of dendritic spatial tuning in single CA1PNs

We reasoned that if ICR regulates synaptic plasticity in vivo, then augmenting its spread and magnitude should affect specific aspects of dendritic feature selectivity in CA1PNs. These effects would in turn provide insight into the endogenous function of ICR. We thus surveyed spatial tuning properties of apical and basal dendrites with respect to their cognate soma in individual *Pdzd8* KO and WT CA1PNs. Because optogenetically induced PFs represented only a fraction of those observed across all 4 days (Fig. 2, A and B), and induced PFs shared similar characteristics with spontaneous PFs (fig. S4, E to G), we initially analyzed PFs regardless of their location relative to prior light-emitting diode (LED) stimulation. In *Pdzd8* KO cells with augmented ICR, both apical and basal dendritic activity showed increased overall spatial tuning (Fig. 2C and supplementary materials and methods). *Pdzd8* KO apical and basal "place dendrites," i.e., dendrites in which PFs were detected, fired more reliably upon the animal's traversal of their PFs (Fig. 2D), whereas basal place dendrites fired more selectively within their PFs (Fig. 2E). Increasing the cytosolic impact of ICR did not significantly affect any measure of somatic spatial tuning (Fig. 2, C to E). This is consistent with the previous finding that increased within-field basal dendritic activity does not portend increased CA1PN somatic activity (*41*) but may also be due to relatively low sample sizes for somatic ROIs; all three metrics in Fig. 2, C to E, trended higher for *Pdzd8* KO CA1PN somata. In conclusion, although augmenting the cytosolic impact of ICR did not affect measures of baseline Ca^{2+} handling or excitability (figs. S6 and S7), the same manipulation promoted feature selectivity in CA1PN apical and basal dendrites.

We next tested whether ICR influences the distribution of dendritic spatial tuning preferences (Fig. 3A). Augmenting ICR by *Pdzd8* KO significantly increased the correlation of spatial tuning curves (TCs) among connected apical and basal dendritic branches (Fig. 3B; see fig. S8 for an illustration of the analytic approach) as well as between apical dendrites and their soma (Fig. 3C). Soma-dendrite TC correlations were unaffected in basal dendrites, although WT basal dendrites already displayed high dendrite-dendrite and dendrite-soma correlations that may have led to a ceiling effect (Fig. 3, B and C). To exclude dendrites that exhibited minimal spatial tuning to begin with, we next restricted our analysis to place dendrites that belonged to place cells and

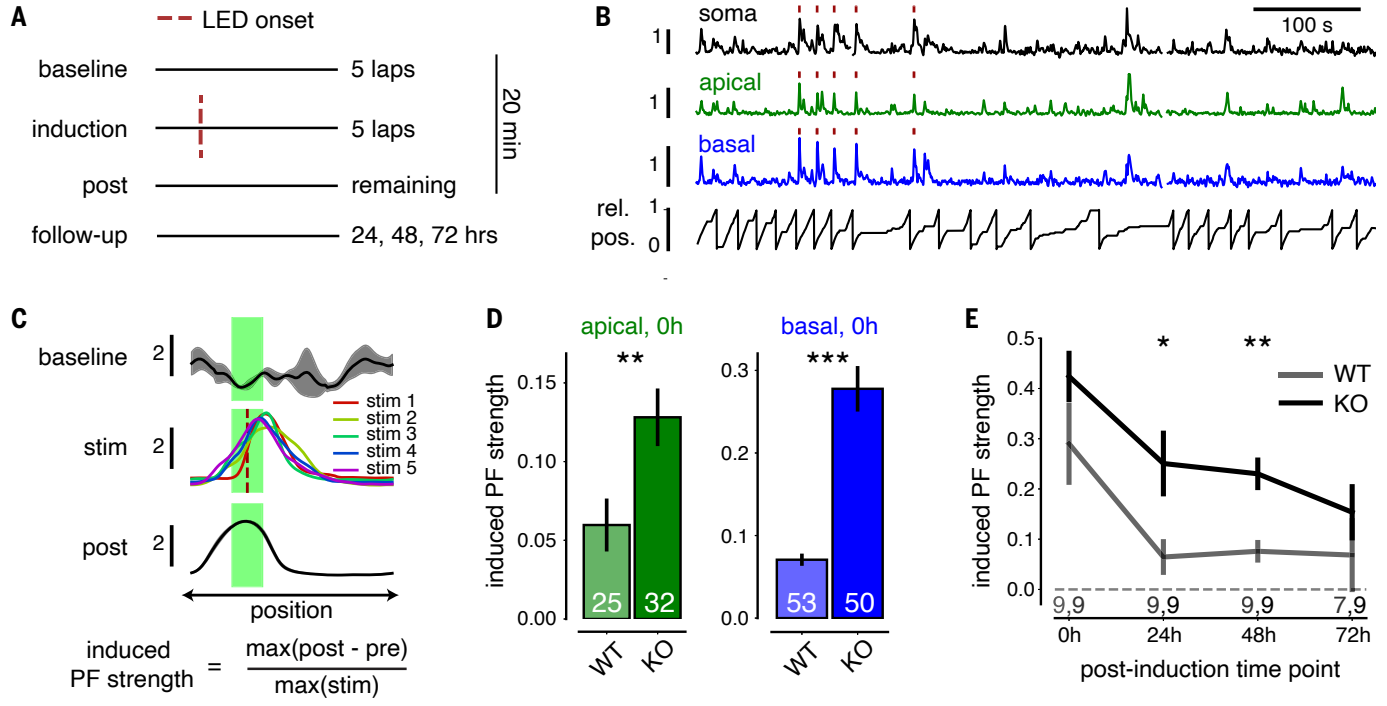

Fig. 5. Dendritic strength and somatic stability of optogenetically induced PFs in single WT and *Pdzd8* KO CA1PNs. (**A**) Paradigm for optogenetic PF induction as in Fig. 1D. (**B**) Traces showing LED-evoked and naturally occurring activity in simultaneously acquired somatic, apical, and basal jGCaMP7b traces from a single CA1PN with relative animal position (rel. pos.) plotted below. LED stimulation during induction laps indicated by red ticks. (**C**) Quantifying strength of induced spatial tuning. Top: Mean somatic dF/F_0 by position from baseline, induction (stim), and post laps for an induced cell with baseline and postactivity shown as mean ± SEM and induction laps shown individually. Red dashed line indicates LED onset and green shaded area denotes "LED zone" used for quantifying induced activity. Bottom: Quantification of induced PF strength. Signals are normalized to maximum LED response to control for cell-to-cell variability in jGCaMP7b expression level, excitability, and/or focality. (**D**) Apical and basal induced PF strength for successfully induced dendrites of WT and *Pdzd8* KO CA1PNs on day 0. Two-sided unpaired *t* tests were used to determine statistical significance. (**E**) Somatic induced PF strength of successfully induced CA1PNs across days. Mixed-effects model with post hoc *t* tests, genotype effect: $F_{(1,16)} = 7.80$, $P < 0.05$; time effect: $F_{(3,46)} = 10.85$, $P < 0.001$; interaction: $F_{(3,46)} = 0.32$, $P > 0.05$. *$P < 0.05$, **$P < 0.01$, ***$P < 0.001$. Error bars and shaded error bands indicate SEM.

calculated the minimum circular distances along the cued belt that separated each dendritic PF from that of its soma. This analysis revealed a previously unappreciated degree of heterogeneity in spatial tuning preference among WT apical dendrites relative to their somata and, by contrast, a clear tendency toward somatic co-tuning in WT basal dendrites (Fig. 3D). Moreover, increased ICR was associated with a significant shift in apical dendritic PFs toward those of their soma; *Pdzd8* KO apical dendrites were as co-tuned to their soma as were WT basal dendrites (Fig. 3D). Consistent with the observation that *Pdzd8* KO selectively affected apical dendrite TC correlations (Fig. 3, B and C), *Pdzd8* KO did not affect basal dendrite-soma co-tuning (Fig. 3D). Dendritic PF specificity did not attenuate with increasing soma-dendrite PF distance (fig. S9) and apical PFs in *Pdzd8* KO CA1PNs displayed increasing specificity the more anti-tuned they were with their somatic PFs (fig. S9A, right). Additionally, neither branch order nor path length predicted dendrite-soma co-tuning (Fig. 3E). Finally, we formally tested the extent of dendrite-soma co-tuning by training a regularized linear model to predict somatic TCs based on those of connected dendrites (Fig. 3F and supplementary materials and methods). This model revealed that apical dendrites with augmented ICR markedly outperformed WT apical dendrites in predicting their somatic TCs, whereas the same manipulation caused basal dendrites to marginally underperform (Fig. 3G).

ICR differentially shapes the subcellular distribution of spatial tuning within single apical and basal dendritic segments

Our results show that the amount of Ca^{2+} released from the ER into the cytosol influences CA1PN dendritic spatial tuning in vivo, but how does the extent of ICR fit into plasticity mechanisms underlying hippocampal feature selectivity? The presence of ER in dendritic spines positively predicts spine head size (*8*), suggesting a role for ICR in spine structural plasticity. In vitro experiments support such a role (*44*–*46*) and further suggest that the spread of ICR along a dendritic branch in part determines which spines will undergo synaptic plasticity (*47*, *48*). Therefore, the spatial extent of ICR along a dendritic branch may ultimately influence local integrative properties underlying dendritic spatial receptive fields in vivo. We investigated how increasing the cytosolic impact of ICR would influence activity and feature selectivity within single dendrites, i.e., across nearby dendritic spines. We subdivided dendritic ROIs into 2-μm segments ("sub-ROIs") and re-extracted, processed, and analyzed sub-ROI signals (Fig. 4A). To account for within-dendrite differences in focality, we normalized activity measures to static mRuby3 signal intensity (see the supplementary materials and methods). Variability in overall activity levels between sub-ROIs was selectively reduced in *Pdzd8* KO apical dendrites (Fig. 4B). Next, we investigated whether increasing ICR altered the spatial features of isolated Ca^{2+} transients along individual dendritic segments (Fig. 3C; see fig. S10A for additional examples). Indeed, genetic amplification of ICR increased the spread of isolated Ca^{2+} transients specifically in apical dendrites (Fig. 4D; fig. S10, B to E; and supplementary materials and methods).

Finally, we calculated TC correlations between all possible combinations of sub-ROIs

and investigated how co-tuning varied between sub-ROIs as a function of the anatomical distance separating them along the dendritic arbor (Fig. 4E). Both apical and basal WT dendrites showed a monotonic decrease in intradendritic TC correlation with distance within single dendritic branches (Fig. 4F). It has been previously suggested (*16*, *49*–*52*), and recently demonstrated (*53*), that feature-correlated inputs are spatially clustered along individual CA1PN dendrites. The distance-dependent drop-off in TC correlations that we observed in dendrites of WT CA1PNs corresponds to the reported distance along which presynaptic inputs were reported to cluster: ~10 μm (*53*). Given the relatively low sensitivity of genetically encoded Ca^{2+} indicators (GECIs), such as jGCaMP7b (*54*), we took this correspondence to indicate that intradendritic GECI signals can provide meaningful insight into how spatially modulated presynaptic inputs are integrated postsynaptically. Similarly, by analyzing spatial tuning within the dendrites of *Pdzd8* KO CA1PNs, we found that increasing ICR strengthened intradendritic TC correlations in both compartments and erased the distance-dependent drop-off in TC correlations specifically within apical dendrites (Fig. 4F).

ICR strengthens dendritic feature selectivity and stabilizes output-level receptive fields

CA1 place cells can gain, lose, remap, or retain their spatial tuning properties. Exposure to a new environment promotes PF formation and remapping (*39*, *55*) whereas, upon repeated exposure to the same environment, subsets of cells stably represent specific locations (*38*, *56*, *57*). Given the role of ICR in controlling the spatial extent of feature selectivity within and across dendrites and in promoting reliability in dendritic PFs, we tested how these input-level PF properties ultimately influence output-level, i.e., somatic, spatial tuning over days. To assess the relative stability of CA1PN spatial tuning over days, we restricted our analysis to activity dynamics within a nominal "LED zone" centered around the location of LED onset during our optogenetic induction protocol (Fig. 5, A to C). We longitudinally tracked somatic activity in the same environment across 72 hours and assessed dendritic activity specifically on day 0 (see the materials and methods). Because PF formation requires both pre- and postsynaptic activity, and only a subset of synapses should receive excitatory presynaptic input at the time of postsynaptic optogenetic stimulation, we expected to induce a fraction of dendrites. Still, dendrites of CA1PNs with augmented ICR were more likely to display optogenetically induced spatial tuning (fig. S11A), revealing a role for ICR in the establishment of dendritic feature selectivity. To measure the strength of induced spatial tuning, we focused specifically on ROIs that were successfully induced (see the materials and methods). We first accounted for cell-to-cell differences in plasmid expression, excitability, and/or focality by normalizing dF/F_0 from each ROI to its peak LED response. We then quantified induced PF strength based on postinduction activity near the location of LED onset relative to a baseline measurement (Fig. 5C).

Both apical and basal dendrites of *Pdzd8* KO CA1PNs displayed stronger induced PFs on day 0 (induction day; Fig. 5D). Although *Pdzd8*

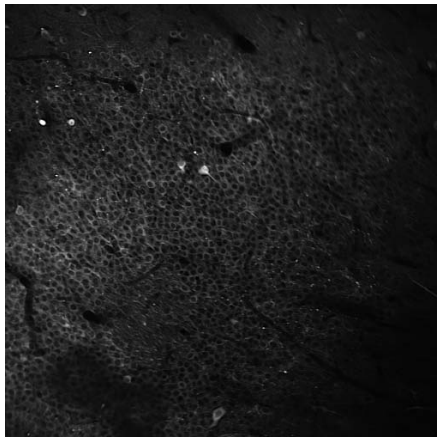

Movie 2. Population GCaMP6f dynamics in the CA1 pyramidal layer during random foraging spatial navigation as in Fig. 6. Frames are motion corrected and shown at actual speed. Data were acquired using two-photon microscopy with a 16× objective lens at 1.2× optical zoom.

KO cell bodies did not show significantly stronger PFs on day 0 relative to WT cells, consistent with our observation that increased dendritic spatial tuning did not significantly translate to output-level PFs (Fig. 2, C to E), induced somatic PFs were more stable over days (Fig. 5E). We considered the possibility that back-propagating action potentials (bAPs) might explain the appearance of strong dendritic PFs in *Pdzd8* KO CA1PNs. If the soma of a *Pdzd8* KO CA1PN fires more robustly near the LED zone, then somatic action potentials may more effectively invade the dendritic arbor and drive increased voltage-dependent Ca^{2+} influx from the extracellular space (*58*). However, dendritic PFs were stronger in *Pdzd8* KO CA1PNs on day 0, when somatic PF strengths were similar (Fig. 5, D and E). Additionally, dendritic proximity to soma did not predict soma-dendrite co-tuning (Fig. 3E). Therefore, we conclude that induced dendritic PF strength is not contaminated by bAPs in our measurements and reflects the degree of local spatial tuning.

ICR shapes PF formation and stabilizes population-level spatial representations

To more rigorously assess the impact of increasing ICR on output-level feature selectivity, and to do so in the context of naturally occurring spatial tuning, we imaged large, intermingled populations of *Pdzd8* KO and WT CA1PN cell bodies (Movie 2 and fig. S12D; see the materials and methods for classification strategy) as mice navigated a familiar cued treadmill belt over 5 consecutive days (Fig. 6, A to C). ROIs were registered across days for longitudinal monitoring of activity dynamics and spatial tuning (Fig. 6C, bottom, and fig. S12). Across two signal extraction and neuropil decontamination approaches, *Pdzd8* KO and WT CA1PNs did not consistently differ in basic Ca^{2+} transient properties or baseline GCaMP6f fluorescence levels (fig. S13). This large-scale, population-level analysis uncovered minor but significant changes in somatic PF properties (fig. S14, A to D) that were not detectable with soma sample sizes in single-cell experiments (Fig. 2, C to E). Consistent with optogenetic PF induction experiments (Fig. 5), somatic TCs of *Pdzd8* KO place cells were more stable day to day relative to WT control place cells (fig. S14G).

One limitation of our single-cell imaging experiments is that their cross-subject design did not permit comparison of PF properties that closely correlate with animal behavior. PF width correlated with peri-formation velocity (fig. S4C), as previously reported (*33*), and the backward shift in PF peak activity (fig. S4D) that characterizes BTSP-mediated PF formation (*33*) covaried with these measures (fig. S11, B to E). Because imaging *Pdzd8* KO and WT CA1PNs within animal controlled for potential behavior-related biases, we sought to identify and compare naturally occurring PF formation events from our mixed-population data. To do this, we devised an automated PF formation detection approach specifically tailored to BTSP-like events (Fig. 6D, fig. S15A, and materials and methods). Augmenting ICR through *Pdzd8* KO did not affect the rate of PF formation across days (Fig. 6E). By assessing place cell TCs relative to the date of PF formation, we again observed that *Pdzd8* KO stabilized spatial TCs of newly formed PFs over days (Fig. 6F). We next assessed PF peak shifts by aligning postformation TCs to the location of PF formation (Fig. 6G and materials and methods). In contrast to WT control CA1PNs, which displayed the backward shift previously established (*33*) and observed in single-cell optogenetic PF induction experiments (fig. S4D and fig. S11E), *Pdzd8* KO CA1PNs with augmented ICR showed no discernable post-formation shift on average (Fig. 6H; see fig. S15B for additional examples). Finally, whereas PF width correlated with peri-formation velocity in both populations, *Pdzd8* KO CA1PN PF widths increased more sharply with velocity and exceeded those of WT control CA1PNs on the whole (Fig. 6, I and J).

Discussion

We found that release of Ca^{2+} from the ER plays a key role in synaptic plasticity mechanisms underlying dendritic receptive field formation, regulating feature selectivity at multiple levels of organization from intra- and interdendritic levels to dendrite-soma co-tuning. These dendritic functions coalesce to govern multiple properties of output-level spatial tuning. The combination of approaches that we developed offers new insights into how ICR participates in PF formation. Based on the impact of increased ICR on two PF characteristics that are specifically influenced by animal behavior during plasticity induction, PF width and peak shift, we conclude that ICR plays an active role in the emergence of cellular feature selectivity in the hippocampus. Consistent with its dependence on voltage-gated Ca^{2+} entry (*59*), ICR appears to operate downstream of plateau potential initiation: Somatic PF stability was improved both in spontaneously occurring and in optogenetically induced PFs, in which plateau potentials and their associated global Ca^{2+} influx (*32*, *60*) are obviated by direct optogenetic depolarization.

It may seem counterintuitive that the spread of ICR would be important if plateau potentials (or optogenetic stimulation) already involve global Ca^{2+} influx from the extracellular space. However, voltage-gated influx of extracellular Ca^{2+} associated even with high

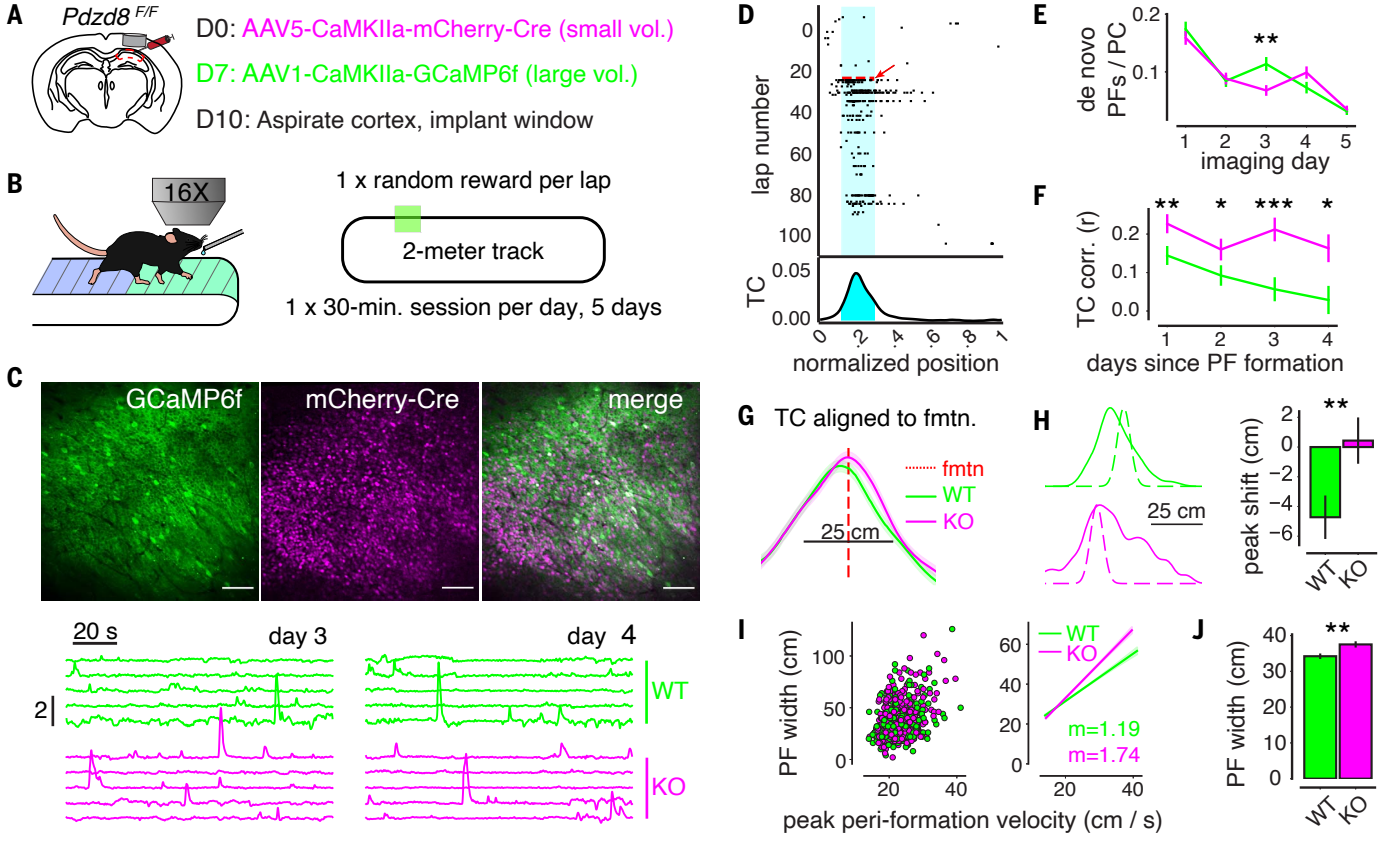

Fig. 6. Large-scale, mixed-population imaging of WT and *Pdzd8* KO CA1PNs implicates intracellular Ca^{2+} release in the formation and stability of output-level feature selectivity. (**A**) Viral strategy. AAV encoding mCherry-Cre fusion protein was injected days before GECI-encoding AAV at low volume to allow for recombination/protein clearance and robust mCherry signal. (**B**) Signals were acquired at 16× (1.2 to 1.5× optical zoom) during a head-fixed spatial navigation paradigm with randomly located reward. Identical fields of view (FoVs) were imaged across 5 consecutive days (see fig. S12). N = 2719 WT and 3260 KO cells from six mice. (**C**) Top: FoVs showing GCaMP6f (left) and mCherry-Cre (middle) expression with overlay (right). Scale bar, 100 μm. Bottom: GCaMP6f traces from the same *Pdzd8* KO (magenta) and WT (green) ROIs imaged on separate days. Vertical scale bar represents dF/F_0. (**D**) Plot showing automated detection of de novo PF formation event. Top: Deconvolved events (black ticks) plotted by lap number and position along cued belt. Red dashed line and arrow indicate detected formation lap with PF bounds shaded in cyan. Bottom: TC for above raster plot with PF shaded in cyan. (**E**) Rates of de novo PF formation over days for all place cells. Two-way ANOVA with post hoc t tests, genotype effect: $F_{(1,1808)}$ = 0.72, P > 0.05; time effect: $F_{(4,7806)}$ = 46.88, P < 0.001; interaction: $F_{(4,7806)}$ = 3.16, P < 0.05. (**F**) TC correlations (TC corrs) over days from *Pdzd8* KO and WT CA1PNs that displayed de novo PF formation events relative to the day of formation. Two-way ANOVA with post hoc t tests, genotype effect: $F_{(1,673)}$ = 24.78, P < 0.001; time effect: $F_{(3,2016)}$ = 3.36, P < 0.05; interaction: $F_{(3,2016)}$ = 0.99, P > 0.05. (**G**) Mean, postformation TCs from all detected de novo events, aligned to where PFs were initially formed (see the supplementary materials and methods). (**H**) Left: Example *Pdzd8* WT (green) and KO (magenta) postformation TCs (solid line) overlaid onto TC from formation lap (dashed line). Right: Quantification of peak shift, i.e., distance between peaks of formation and postformation TCs. N = 350 and 369 formation events from *Pdzd8* WT and KO CA1PNs, respectively. CA1PNs with multiple PFs were excluded from analysis. (**I**) Relationship between periformation velocity and resultant PF width for *Pdzd8* WT (green, N = 366) and KO (magenta, N = 373) events across six mice. Left: Scatter plot of all events. Right: Least-squares linear fits of data shown on left with corresponding slopes (m) (r_{WT} = 0.33, P < 001; r_{KO} = 0.41, P < 0.001). (**J**) Widths of all de novo PFs. Error bars represent SEM. Boxes range from lower to upper quartiles with line at median; whiskers show range of data within 1.5 * (Q3 − Q1) of box boundaries. Distributions were compared using two-sided unpaired t tests and Mann-Whitney U tests. *P < 0.05, **P < 0.01, ***P < 0.001.

degrees of spiking exerts a minor impact on intracellular Ca^{2+} concentrations ($[Ca^{2+}]_i$) relative to ICR (*10*, *14*). Consistent with the high threshold for ICR engagement (*5*, *10*–*13*, *59*), and thus its presumed rarity in vivo, *Pdzd8* deletion did not alter basic excitability or Ca^{2+}-handling properties that might otherwise have obfuscated interpretation of GECI signals. Therefore, altered ICR alone is unlikely to account for our observations using GCaMP to monitor voltage-dependent influx of extracellular Ca^{2+}. Rather, we propose that ICR occurs relatively infrequently in vivo—during plateau potentials in CA1PNs, for example—and participates in the induction of synaptic plasticity. In this context, our results suggest that augmented ICR lastingly modifies dendritic integrative properties.

The widening of *Pdzd8* KO PFs specifically in the forward direction suggests that a prolonged ICR-driven Ca^{2+} signal potentiates more dendritic spines receiving input after plateau potential onset. Consistent with a broadening of potentiated inputs, we found that spatial tuning preferences were more uniform within single apical dendritic segments of *Pdzd8* KO CA1PNs. It was recently established that feature-correlated presynaptic inputs are spatially clustered along CA1PN dendrites, i.e., that neighboring spines tend to receive input corresponding to similar sensory experiences (*53*). We observed a postsynaptic vestige of this phenomenon in WT dendritic segments: Intradendritic TC correlations systematically decreased with intervening distance. This drop-off began after ~10 μm, the same distance across which correlated presynaptic inputs were previously reported to cluster. The fact that augmenting ICR abrogated this distance-dependent decorrelation in apical dendrites and widened output-level PFs additionally suggests that the diffusion of ER-released Ca^{2+} along a dendritic shaft may influence the number of spines co-potentiated during plasticity induction. Although previous in vitro studies directly support such a model (*47*, *48*), ICR may also regulate intradendritic spatial tuning through branch-specific plasticity of dendritic excitability (*61*). Given that *Pdzd8* KO did not affect baseline GCaMP fluorescence or the amplitude of isolated events in dendritic spines and shafts, it is unlikely that acute effects of augmented ICR, which again is presumed to be relatively infrequent in vivo, influence intradendritic spatial tuning. In addition to broadening the anatomical distribution of dendritic feature selectivity, increasing ICR also strengthened spatial tuning: Dendritic and somatic PFs were more specific and sensitive, whereas somatic PFs were also more durable over time in the face of constant representational turnover within CA1 (*38*, *62*). Finally, the substantial impact of increasing ICR on dendrite-dendrite and soma-dendrite co-tuning, again specifically within the apical arbor, indicates that ICR operates on multiple spatial scales (*12*, *13*, *19*) to shape output-level receptive fields.

A role for ICR in the emergence of feature selectivity is further supported by the velocity-dependent nature in which augmenting ICR widened PFs. CA1PN synapses require temporally correlated pre- and postsynaptic activity to undergo plasticity (*33*, *60*, *63*). Higher running speeds positively modulate the rate of presynaptic input onto CA1PNs (*64*, *65*), increasing the pool of synapses eligible for potentiation during PF formation in vivo and hence the velocity-PF width relationship (*33*). Therefore, whereas unperturbed ICR may reach and potentiate most eligible inputs at lower velocities, increased ICR would be predicted to more comprehensively engage larger pools of eligible connections generated during bouts of increased running speed. We acknowledge that normative statements regarding ICR function are difficult to make based on a gain-of-function manipulation. However, our mild, ~50% augmentation (*9*) of $[Ca^{2+}]_i$ associated with ICR may well fall within the range of physiological variability, because the magnitudes of individual ICR events are known to vary according to a number of factors (*10*, *12*, *13*, *16*, *59*, *66*, *67*). Therefore, although we acknowledge that our findings pertain to one specific plasticity mechanism underlying PF formation, we propose ICR magnitude, as regulated by ER-mitochondria contact sites (*9*), as a general mechanism influencing the distribution of synaptic plasticity induction in vivo.

Independent of ICR, we found that apical dendrites of CA1PNs have a great deal of functional autonomy from the soma. Apical CA1PN dendrites have been the subject of extensive in vitro research due to their presumed central role in hippocampus-dependent learning, but their in vivo activity had remained elusive. The broadly distributed tuning preferences observed across apical dendrites in single WT CA1PNs could not be explained by path length from soma or by branch order, nor did soma-basal dendritic co-tuning track with these morphological properties. This is consistent with a prior observation that co-firing between basal dendrites and their soma does not depend on intervening distance (*41*) and indicates that somatic AP back-propagation does not appreciably influence soma-dendrite co-tuning, at least across the relatively broad ranges of branch order and path length that we sampled. Nor were anti-tuned dendritic PFs of lesser quality: PF specificity did not track with the degree of soma-dendrite co-tuning. Therefore, similar to pyramidal neurons of various sensory cortices (*68*–*70*), CA1PNs are able to integrate diverse dendritic tuning preferences into single, clean receptive fields. How this aspect of feature selectivity emerges remains poorly understood.

By contrast, basal dendrites showed stronger correlation with somatic tuning. This may have been due to a true biological difference between apical and basal dendrites of CA1PNs. Alternatively, somatic action potentials may invade basal dendrites more efficiently because their relatively closer proximity to the soma would mitigate distance-dependent attenuation of bAPs (*58*). In this case, correlated voltage-dependent Ca^{2+} influx from the extracellular space would indeed be expected. However, given that soma-dendrite co-tuning was predicted by neither branch order nor path length in either dendritic compartment, we propose that apical dendritic tuning is more decoupled from somatic tuning relative to basal dendrites and that ICR, as regulated by mitochondrial Ca^{2+} buffering, contributes to this functional compartmentalization. The compartment-specific nature of ICR's role in plasticity intersects with the CA1PN input structure in a potentially powerful way. Given that apical and basal dendrites receive synaptic input from unique combinations of afferent circuits carrying distinct streams of information (*71*), compartment-specific action by ER may allow selected features of experience to preferentially influence learning.

Methods Summary

See the supplementary materials for full materials and methods information.

Animals

All experiments were conducted in accordance with National Institutes of Health guidelines and were approved by the Columbia University Institutional Animal Care and Use Committee under protocols AC-AABF6554, AC-AAAX1460, and AC-AAAO0850. Animal health and welfare were supervised by a designated veterinarian. Columbia University animal facilities comply with all appropriate standards of care, including cage conditions, space per animal, temperature, light, humidity, food, and water. Adult (postnatal day 60 or older) male and female $Pdzd8^{F/F}$ and WT mice, fully backcrossed to the C57Bl/6 genetic background, were used for all experiments. The authors are not aware of an influence of sex on the measures of interest to this study.

Plasmids

pCAG-Cre was generated in the laboratory of F.P. as previously described (*72*). pAAV-CAG-FLEX-jGCaMP7b-WPRE was obtained from Addgene (#104497). pCAG-FLEX-eGFP was a gift from A. Maximov (Scripps). pAAV-CaMKIIa-bReaChes-mRuby3 was subcloned from pAAV-CaMKIIa-bReaChes-EYFP (gift from K. Deisseroth) by excising the EYFP

sequence and replacing it with an mRuby3 fragment (cloned from pAAV-CAG-mRuby3-WPRE, Addgene #107744). pCAG-NES-jRGECO1a was generated by subcloning an NES-jRGECO1a insert (from pAAV-Syn-NES-jRGECO1a-WPRE, Addgene #100854) into a pCAG backbone. Subcloning was performed using the In-Fusion cloning kit (Takara Bio).

Single-cell electroporation

To electroporate single CA1PNs with custom plasmid combinations, animals were head-fixed under a two-photon microscope and anesthetized under a ketamine-xylazine mixture with continuous heat source. Sterile 1× phosphate-buffered saline was used to make a grounded solution in the bowl-shaped dental acrylic cap atop the imaging implant. A pipette containing fluorescent plasmid solution was lowered at an angle using a motorized micromanipulator (Scientifica) through the rectangular slit in the imaging coverslip and through the thin silicone protective layer while maintaining positive pipette pressure to avoid clogging. Once in the brain, the pipette was gradually lowered to the CA1 pyramidal layer (Fig. 1A, middle) while continuously expelling low amounts of fluorescent solution to aid visualization under 920-nm, two-photon excitation. As the pipette approached a putative CA1PN, tip resistance was used to monitor proximity. After a small deflection in resistance and while maintaining positive pressure, a train of negative voltage pulses was delivered from a stimulus isolator (AMPI) to the amplifier head stage using a custom-made switch circuit. Successful electroporation was confirmed based on a cell filling with Alexa Fluor dye and retaining the dye after careful pipette retraction (Fig. 1A, middle). Plasmid DNA expression was checked 48 hours later. To ensure successful genetic KO of *Pdzd8* (fig. S1, A to F) and clearance of PDZD8 protein (fig. S1, G and H), imaging experiments were conducted no less than 7 days after electroporation for either $Pdzd8^{F/F}$ or WT control mice. See the supplementary materials and methods for additional details.

Animal behavior

Mice ran along a spatially cued, 2-m treadmill belt under "random foraging" conditions in which water reward was delivered at a pseudorandom location once per lap. Initial delivery was nonoperant and was followed by a 3-s period during which the animal could receive an additional operant water reward by licking with a 50% reward rate. Mice were habituated on the same cued belts used for experiments for 1 to 2 days with training sessions under the in vivo imaging setup before data acquisition. For each mouse, the belt was never changed across days within a given experiment and was calibrated to the exact same length each day using a fixed landmark of blackout tape, an infrared beam, and custom software.

In vivo two-photon Ca^{2+} imaging

All imaging experiments described in the figures were performed using a two-photon 8-kHz resonant scanning microscope (Bruker) equipped with a Chameleon Ultra II Ti:sapphire laser (Coherent), tuned to 920 nm for green wavelength excitation, and a Fidelity-2 (Coherent) laser fixed at 1070 nm for red excitation. Excitation pathways were separately controlled and combined at the microscope. Green and red fluorescence were separated with an emission filter set (HQ525/70m-2p, HQ607/45m-2p, 575dcxr, Chroma Technology) and collected using channel-dedicated GaAsP (7422P-40, Hamamatsu Photonics) photomultiplier tubes (PMTs). A custom dual-stage preamplifier (1.4 × 105 dB, Bruker) was used to amplify signals before digitization. For details on the spine-level imaging experiments described in fig. S6, G to J, and movie S1, see the supplementary materials and methods.

Single-cell optogenetic PF induction

Induction sessions constituted the first imaging day of each single-cell imaging experiment. After a baseline period of five laps, a 1-s LED photostimulation was triggered at a fixed location along the treadmill belt for five consecutive laps. If preexisting somatic spatial tuning was evident (as visually assessed offline before baseline periods), LED location was set to be as far away as possible from the existing putative PF. To deliver LED photostimulation while simultaneously acquiring jGCaMP7b Ca^{2+} dynamics, 620-nm light from a C-mounted ultra-fast, ultra-high-powered LED (UHP-T-620-SR, Prizmatix) was passed through a dichroic mirror, allowing red light to pass into the objective lens back aperture while deflecting emitted green photons to their dedicated PMT (Fig. 1B, left). The red channel used to acquire mRuby3 signals was manually switched off during photostimulation. LED was triggered by a custom "Pockels-blanking" circuit that relayed an inverted Pockels cell blanking signal that was briefly activated during Y-galvonometer flyback periods and during toggling of the piezoelectric device. This approach allowed for high-powered (30 to 40 mW at sample), pulsed LED stimulation during image acquisition while protecting PMTs from potentially saturating LED photons that might otherwise be incompletely deflected from the green collection channel given high LED power. After optogenetic PF induction, the remainder of the 20-min imaging session was used to acquire postinduction data. All cells were tracked for 72 hours, except for two WT cells that died at the 72-hour mark (Fig. 5E and table S1). Of the 16 induction experiments performed, all but three sessions involved one CA1PN. Two WT experiments and one KO experiment involved two electroporated CA1PNs in the same field of view.

Detecting spontaneous PF formation events

To detect de novo PF formation events, we quantified the number of events falling within a search window ("hits") that corresponded to the PF bounds plus a forward extension of 20 cm to account for an expected backward shift in PF activity relative to formation location (*33*). We then used an $N = 2$ Gaussian mixture model (GMM) to initially differentiate between putative "PRE" and "POST" laps relative to PF formation. For each detected PF, the GMM was fit to a two-feature matrix with columns representing (i) a rolling average (weighted by Bartlett window) of hit counts by lap and (ii) lap numbers multiplied by exponentially decaying weights. The GMM fit was randomly initiated 1000 times for each PF, and the best fit was taken. The PF was assumed to have existed before session start if (i) the model did not converge, (ii) all laps were assigned to a single component, or (iii) the mean hit/lap rate in PRE laps was >1. These events were discarded. Next, we searched for a large Ca^{2+} transient (≥1 SD above mean amplitude) representing a putative PF-forming plateau potential. If a candidate transient was identified within 10 laps on either side of the first POST lap, then the first such event was taken as the PF-forming event. If no such candidate event was identified, then the putative de novo PF was discarded. To validate detected PF formation events, five conditions were imposed: (i) the same cell did not express an overlapping PF on the previous day, (ii) the hit rates in PRE versus POST laps were significantly different by the Mann-Whitney *U* test, (iii) the place cell fired within its PF on at least a third of POST laps, (iv) place cell events showed at least 35% specificity to the PF after formation, and (v) the PF did not form earlier than lap 10 to further mitigate the possibility that it had formed before imaging. For each PF-forming Ca^{2+} transient, we documented the corresponding lap, 2-cm spatial bin, and the imaging frame at which the event reached peak amplitude for future analyses. See fig. S14A for example performance and the supplementary materials and methods for additional details and rationale.

Analyzing PF formation events

For optogenetically induced PFs in single cells, an "LED zone" was defined to operationalize what activity should be considered induced. The LED zone was defined as a symmetric window, with a 15 cm radius, centered on LED onset position (Fig. 5C, green shaded area) on a cued, 2-m treadmill belt. For each induction experiment, spatial tuning heatmaps

were calculated (as described in the supplementary materials and methods) based on preinduction (baseline), peri-induction, and postinduction laps using dF/F_0. Induction efficacy was calculated as the maximum difference between postinduction and baseline TCs within the LED zone. Baseline and postinduction TCs to the maximum observed LED response for a given ROI are shown in Fig. 5C. An ROI was considered "induced" if its mean postinduction dF/F_0 exceeded baseline dF/F_0 in at least one position bin (50 4-cm bins were used) within the LED zone. Performation velocity (figs. S4C and S11, B and D) was defined as the mean velocity observed from 1.5 s before and 1.0 s after LED onset during the first induction lap. This temporal window was formulated to capture the bulk of the integral of the asymmetric plasticity kernel underlying BTSP (*32*). For spontaneously occurring PF formation events in the population imaging data, we adjusted our calculation of performation velocity to accommodate the inherent uncertainty in estimating plateau potential onset times based on somatic GCaMP signals. Performation velocity was calculated as the peak velocity within the spatial search window described above on the formation lap. See the supplementary materials and methods for additional details and rationale.

To calculate PF peak shifts, we increased the resolution of spatial bins to 0.5 cm (400 spatial bins per 2-m lap). Large, PF-forming Ca^{2+} transients were localized to the nearest 0.5-cm spatial bin based on the imaging frame corresponding to peak transient amplitude. Postformation TCs were calculated from all laps subsequent to the formation lap within an imaging session. Peak shifts were defined as the distance between peaks of formation and postformation TCs. Widths of de novo PFs were calculated using events from all laps.

REFERENCES AND NOTES

1. P. L. Greer, M. E. Greenberg, From synapse to nucleus: Calcium-dependent gene transcription in the control of synapse development and function. *Neuron* **59**, 846–860 (2008). doi: 10.1016/j.neuron.2008.09.002; pmid: 18817726
2. G. J. Stuart, N. Spruston, Dendritic integration: 60 years of progress. *Nat. Neurosci.* **18**, 1713–1721 (2015). doi: 10.1038/nn.4157; pmid: 26605882
3. M. Häusser, N. Spruston, G. J. Stuart, Diversity and dynamics of dendritic signaling. *Science* **290**, 739–744 (2000). doi: 10.1126/science.290.5492.739; pmid: 11052929
4. E. Nanou, W. A. Catterall, Calcium channels, synaptic plasticity, and neuropsychiatric disease. *Neuron* **98**, 466–481 (2018). doi: 10.1016/j.neuron.2018.03.017; pmid: 29723500
5. H. Takechi, J. Eilers, A. Konnerth, A new class of synaptic response involving calcium release in dendritic spines. *Nature* **396**, 757–760 (1998). doi: 10.1038/25547; pmid: 9874373
6. E. G. Gray, Axo-somatic and axo-dendritic synapses of the cerebral cortex: An electron microscope study. *J. Anat.* **93**, 420–433 (1959). pmid: 13829103
7. A. Peters, S. L. Palay, H. deF. Webster, *Fine Structure of the Nervous System: Neurons and Their Supporting Cells* (Oxford Univ. Press, 1991).
8. J. Spacek, K. M. Harris, Three-dimensional organization of smooth endoplasmic reticulum in hippocampal CA1 dendrites and dendritic spines of the immature and mature rat. *J. Neurosci.* **17**, 190–203 (1997). doi: 10.1523/JNEUROSCI.17-01-00190.1997; pmid: 8987748
9. Y. Hirabayashi *et al*., ER-mitochondria tethering by PDZD8 regulates Ca^{2+} dynamics in mammalian neurons. *Science* **358**, 623–630 (2017). doi: 10.1126/science.aan6009; pmid: 29097544
10. T. Nakamura, J.-G. Barbara, K. Nakamura, W. N. Ross, Synergistic release of Ca2+ from IP3-sensitive stores evoked by synaptic activation of mGluRs paired with backpropagating action potentials. *Neuron* **24**, 727–737 (1999). doi: 10.1016/S0896-6273(00)81125-3; pmid: 10595522
11. T. Nakamura *et al*., Inositol 1,4,5-trisphosphate (IP_3)-mediated Ca^{2+} release evoked by metabotropic agonists and backpropagating action potentials in hippocampal CA1 pyramidal neurons. *J. Neurosci.* **20**, 8365–8376 (2000). doi: 10.1523/JNEUROSCI.20-22-08365.2000; pmid: 11069943
12. T. Nakamura, N. Lasser-Ross, K. Nakamura, W. N. Ross, Spatial segregation and interaction of calcium signalling mechanisms in rat hippocampal CA1 pyramidal neurons. *J. Physiol.* **543**, 465–480 (2002). doi: 10.1113/jphysiol.2002.020362; pmid: 12205182
13. M. E. Larkum, S. Watanabe, T. Nakamura, N. Lasser-Ross, W. N. Ross, Synaptically activated Ca^{2+} waves in layer 2/3 and layer 5 rat neocortical pyramidal neurons. *J. Physiol.* **549**, 471–488 (2003). doi: 10.1113/jphysiol.2002.037614; pmid: 12692172
14. W. N. Ross, T. Nakamura, S. Watanabe, M. Larkum, N. Lasser-Ross, Synaptically activated ca2+ release from internal stores in CNS neurons. *Cell. Mol. Neurobiol.* **25**, 283–295 (2005). doi: 10.1007/s10571-005-3060-0; pmid: 16047542
15. M. Nishiyama, K. Hong, K. Mikoshiba, M.-M. Poo, K. Kato, Calcium stores regulate the polarity and input specificity of synaptic modification. *Nature* **408**, 584–588 (2000). doi: 10.1038/35046067; pmid: 11117745
16. K. F. Lee, C. Soares, J. P. Thivierge, J. C. Béïque, Correlated synaptic inputs drive dendritic calcium amplification and cooperative plasticity during clustered synapse development. *Neuron* **89**, 784–799 (2016). doi: 10.1016/j.neuron.2016.01.012; pmid: 26853305
17. F. W. Johenning *et al*., Ryanodine receptor activation induces long-term plasticity of spine calcium dynamics. *PLOS Biol.* **13**, e1002181 (2015). doi: 10.1371/journal.pbio.1002181; pmid: 26098891
18. S. Bardo, M. G. Cavazzini, N. Emptage, The role of the endoplasmic reticulum Ca2+ store in the plasticity of central neurons. *Trends Pharmacol. Sci.* **27**, 78–84 (2006). doi: 10.1016/j.tips.2005.12.008; pmid: 16412523
19. N. Emptage, T. V. Bliss, A. Fine, Single synaptic events evoke NMDA receptor-mediated release of calcium from internal stores in hippocampal dendritic spines. *Neuron* **22**, 115–124 (1999). doi: 10.1016/S0896-6273(00)80683-2; pmid: 10027294
20. K. Svoboda, Z. F. Mainen, Synaptic [Ca2+]: Intracellular stores spill their guts. *Neuron* **22**, 427–430 (1999). doi: 10.1016/S0896-6273(00)80698-4; pmid: 10197523
21. C. R. Rose, A. Konnerth, Stores not just for storage. intracellular calcium release and synaptic plasticity. *Neuron* **31**, 519–522 (2001). doi: 10.1016/S0896-6273(01)00402-0; pmid: 11545711
22. A. Handler *et al*., Distinct dopamine receptor pathways underlie the temporal sensitivity of associative learning. *Cell* **178**, 60–75.e19 (2019). doi: 10.1016/j.cell.2019.05.040; pmid: 31230716
23. A. H. Sharp *et al*., Differential immunohistochemical localization of inositol 1,4,5-trisphosphate- and ryanodine-sensitive Ca2+ release channels in rat brain. *J. Neurosci.* **13**, 3051–3063 (1993). doi: 10.1523/JNEUROSCI.13-07-03051.1993; pmid: 8392539
24. M. Migliore, M. Ferrante, G. A. Ascoli, Signal propagation in oblique dendrites of CA1 pyramidal cells. *J. Neurophysiol.* **94**, 4145–4155 (2005). doi: 10.1152/jn.00521.2005; pmid: 16293591
25. M. Andreasen, J. D. C. Lambert, Factors determining the efficacy of distal excitatory synapses in rat hippocampal CA1 pyramidal neurones. *J. Physiol.* **507**, 441–462 (1998). doi: 10.1111/j.1469-7793.1998.441bt.x; pmid: 9518704
26. J. C. Magee, Dendritic hyperpolarization-activated currents modify the integrative properties of hippocampal CA1 pyramidal neurons. *J. Neurosci.* **18**, 7613–7624 (1998). doi: 10.1523/JNEUROSCI.18-19-07613.1998; pmid: 9742133
27. G. K. Pyapali, A. Sik, M. Penttonen, G. Buzsaki, D. A. Turner, Dendritic properties of hippocampal CA1 pyramidal neurons in the rat: Intracellular staining in vivo and in vitro. *J. Comp. Neurol.* **391**, 335–352 (1998). doi: 10.1002/(SICI)1096-9861(19980216)391:3<335::AID-CNE4>3.0.CO;2-2; pmid: 9492204
28. M. T. Harnett, J. K. Makara, N. Spruston, W. L. Kath, J. C. Magee, Synaptic amplification by dendritic spines enhances input cooperativity. *Nature* **491**, 599–602 (2012). doi: 10.1038/nature11554; pmid: 23103868
29. N. Spruston, Pyramidal neurons: Dendritic structure and synaptic integration. *Nat. Rev. Neurosci.* **9**, 206–221 (2008). doi: 10.1038/nrn2286; pmid: 18270515
30. J. O'Keefe, J. Dostrovsky, The hippocampus as a spatial map. Preliminary evidence from unit activity in the freely-moving rat. *Brain Res.* **34**, 171–175 (1971).
31. J. O'Keefe, L. Nadel, *The Hippocampus As a Cognitive Map* (Clarendon Press, 1978).
32. K. C. Bittner *et al*., Conjunctive input processing drives feature selectivity in hippocampal CA1 neurons. *Nat. Neurosci.* **18**, 1133–1142 (2015). doi: 10.1038/nn.4062; pmid: 26167906
33. K. C. Bittner, A. D. Milstein, C. Grienberger, S. Romani, J. C. Magee, Behavioral time scale synaptic plasticity underlies CA1 place fields. *Science* **357**, 1033–1036 (2017). doi: 10.1126/science.aan3846; pmid: 28883072
34. J. C. Magee, C. Grienberger, Synaptic plasticity forms and functions. *Annu. Rev. Neurosci.* **43**, 95–117 (2020). doi: 10.1146/annurev-neuro-090919-022842; pmid: 32075520
35. J. de Juan-Sanz *et al*., Axonal endoplasmic reticulum Ca^{2+} content controls release probability in CNS nerve terminals. *Neuron* **93**, 867–881.e6 (2017). doi: 10.1016/j.neuron.2017.01.010; pmid: 28162809
36. N. B. Danielson *et al*., Sublayer-specific coding dynamics during spatial navigation and learning in hippocampal area CA1. *Neuron* **91**, 652–665 (2016). doi: 10.1016/j.neuron.2016.06.020; pmid: 27397517
37. J. D. Zaremba *et al*., Impaired hippocampal place cell dynamics in a mouse model of the 22q11.2 deletion. *Nat. Neurosci.* **20**, 1612–1623 (2017). doi: 10.1038/nn.4634; pmid: 28869582
38. Y. Ziv *et al*., Long-term dynamics of CA1 hippocampal place codes. *Nat. Neurosci.* **16**, 264–266 (2013). doi: 10.1038/nn.3329; pmid: 23396101
39. J. B. Priestley, J. C. Bowler, S. V. Rolotti, S. Fusi, A. Losonczy, Signatures of rapid synaptic learning in the hippocampus during novel experiences [Preprint]. bioRxiv 450956 (2021); doi: 10.1101/2021.07.02.450956
40. C. Grienberger, J. C. Magee, Entorhinal cortex directs learning-related changes in CA1 representations [Preprint]. bioRxiv 472158 (2021); doi: 10.1101/2021.12.10.472158
41. M. E. Sheffield, D. A. Dombeck, Calcium transient prevalence across the dendritic arbour predicts place field properties. *Nature* **517**, 200–204 (2015). doi: 10.1038/nature13871; pmid: 25363782
42. M. E. J. Sheffield, M. D. Adoff, D. A. Dombeck, Increased prevalence of calcium transients across the dendritic arbor during place field formation. *Neuron* **96**, 490–504.e5 (2017). doi: 10.1016/j.neuron.2017.09.029; pmid: 29024668
43. S. V. Rolotti, H. Blockus, F. T. Sparks, J. B. Priestley, A. Losonczy, Reorganization of CA1 dendritic dynamics by hippocampal sharp-wave ripples during learning. *Neuron* S0896-6273(21)01034-5 (2022). doi: 10.1016/j.neuron.2021.12.017; pmid: 35041805
44. P. J. Dittmer, A. R. Wild, M. L. Dell'Acqua, W. A. Sather, STIM1 Ca^{2+} sensor control of L-type Ca^{2+}-channel-dependent dendritic spine structural plasticity and nuclear signaling. *Cell Rep.* **19**, 321–334 (2017). doi: 10.1016/j.celrep.2017.03.056; pmid: 28402855
45. N. Holbro, A. Grunditz, T. G. Oertner, Differential distribution of endoplasmic reticulum controls metabotropic signaling and plasticity at hippocampal synapses. *Proc. Natl. Acad. Sci. U.S.A.* **106**, 15055–15060 (2009). doi: 10.1073/pnas.0905110106; pmid: 19706463
46. M. Dur-e-Ahmad, M. Imran, A. Gul, Calcium dynamics in dendritic spines: A link to structural plasticity. *Math. Biosci.* **230**, 55–66 (2011). doi: 10.1016/j.mbs.2011.01.002; pmid: 21295598
47. P. J. Dittmer, M. L. Dell'Acqua, W. A. Sather, Synaptic crosstalk conferred by a zone of differentially regulated Ca^{2+} signaling in the dendritic shaft adjoining a potentiated spine. *Proc. Natl. Acad. Sci. U.S.A.* **116**, 13611–13620 (2019). doi: 10.1073/pnas.1902461116; pmid: 31209051
48. E. A. Finch, G. J. Augustine, Local calcium signalling by inositol-1,4,5-trisphosphate in Purkinje cell dendrites. *Nature* **396**, 753–756 (1998). doi: 10.1038/25541; pmid: 9874372
49. S. Druckmann *et al*., Structured synaptic connectivity between hippocampal regions. *Neuron* **81**, 629–640 (2014). doi: 10.1016/j.neuron.2013.11.026; pmid: 24412418
50. T. Kleindienst, J. Winnubst, C. Roth-Alpermann, T. Bonhoeffer, C. Lohmann, Activity-dependent clustering of functional

synaptic inputs on developing hippocampal dendrites. *Neuron* **72**, 1012–1024 (2011). doi: 10.1016/j.neuron.2011.10.015; pmid: 22196336
51. O. Kwon, L. Feng, S. Druckmann, J. Kim, Schaffer collateral inputs to CA1 excitatory and inhibitory neurons follow different connectivity rules. *J. Neurosci.* **38**, 5140–5152 (2018). doi: 10.1523/JNEUROSCI.0155-18.2018; pmid: 29728449
52. N. Takahashi *et al*., Locally synchronized synaptic inputs. *Science* **335**, 353–356 (2012). doi: 10.1126/science.1210362; pmid: 22267814
53. M. D. Adoff *et al*., The functional organization of excitatory synaptic input to place cells. *Nat. Commun.* **12**, 3558 (2021). doi: 10.1038/s41467-021-23829-y; pmid: 34117238
54. H. Dana *et al*., High-performance calcium sensors for imaging activity in neuronal populations and microcompartments. *Nat. Methods* **16**, 649–657 (2019). doi: 10.1038/s41592-019-0435-6; pmid: 31209382
55. C. Dong, A. D. Madar, M. E. J. Sheffield, Distinct place cell dynamics in CA1 and CA3 encode experience in new environments. *Nat. Commun.* **12**, 2977 (2021). doi: 10.1038/s41467-021-23260-3; pmid: 34016996
56. T. Hainmueller, M. Bartos, Parallel emergence of stable and dynamic memory engrams in the hippocampus. *Nature* **558**, 292–296 (2018). doi: 10.1038/s41586-018-0191-2; pmid: 29875406
57. N. R. Kinsky, D. W. Sullivan, W. Mau, M. E. Hasselmo, H. B. Eichenbaum, Hippocampal Place Fields Maintain a Coherent and Flexible Map across Long Timescales. *Curr. Biol.* **28**, 3578–3588.e6 (2018). doi: 10.1016/j.cub.2018.09.037; pmid: 30393037
58. N. L. Golding, W. L. Kath, N. Spruston, Dichotomy of action-potential backpropagation in CA1 pyramidal neuron dendrites. *J. Neurophysiol.* **86**, 2998–3010 (2001). doi: 10.1152/jn.2001.86.6.2998; pmid: 11731556
59. M. Kano, O. Garaschuk, A. Verkhratsky, A. Konnerth, Ryanodine receptor-mediated intracellular calcium release in rat cerebellar Purkinje neurones. *J. Physiol.* **487**, 1–16 (1995). doi: 10.1113/jphysiol.1995.sp020857; pmid: 7473240
60. H. Takahashi, J. C. Magee, Pathway interactions and synaptic plasticity in the dendritic tuft regions of CA1 pyramidal neurons. *Neuron* **62**, 102–111 (2009). doi: 10.1016/j.neuron.2009.03.007; pmid: 19376070
61. A. Losonczy, J. K. Makara, J. C. Magee, Compartmentalized dendritic plasticity and input feature storage in neurons. *Nature* **452**, 436–441 (2008). doi: 10.1038/nature06725; pmid: 18368112
62. J. S. Lee, J. J. Briguglio, J. D. Cohen, S. Romani, A. K. Lee, The statistical structure of the hippocampal code for space as a function of time, context, and value. *Cell* **183**, 620–635.e22 (2020). doi: 10.1016/j.cell.2020.09.024; pmid: 33035454
63. E. Campanac, D. Debanne, Spike timing-dependent plasticity: A learning rule for dendritic integration in rat CA1 pyramidal neurons. *J. Physiol.* **586**, 779–793 (2008). doi: 10.1113/jphysiol.2007.147017; pmid: 18048448
64. K. Diba, G. Buzsáki, Hippocampal network dynamics constrain the time lag between pyramidal cells across modified environments. *J. Neurosci.* **28**, 13448–13456 (2008). doi: 10.1523/JNEUROSCI.3824-08.2008; pmid: 19074018
65. K. Mizuseki, S. Royer, K. Diba, G. Buzsáki, Activity dynamics and behavioral correlates of CA3 and CA1 hippocampal pyramidal neurons. *Hippocampus* **22**, 1659–1680 (2012). doi: 10.1002/hipo.22002; pmid: 22367959
66. O. Garaschuk, Y. Yaari, A. Konnerth, Release and sequestration of calcium by ryanodine-sensitive stores in rat hippocampal neurones. *J. Physiol.* **502**, 13–30 (1997). doi: 10.1111/j.1469-7793.1997.013bl.x; pmid: 9234194
67. S. A. Neymotin *et al*., Neuronal calcium wave propagation varies with changes in endoplasmic reticulum parameters: A computer model. *Neural Comput.* **27**, 898–924 (2015). doi: 10.1162/NECO_a_00712; pmid: 25734493
68. H. Jia, N. L. Rochefort, X. Chen, A. Konnerth, Dendritic organization of sensory input to cortical neurons in vivo. *Nature* **464**, 1307–1312 (2010). doi: 10.1038/nature08947; pmid: 20428163
69. X. Chen, U. Leischner, N. L. Rochefort, I. Nelken, A. Konnerth, Functional mapping of single spines in cortical neurons in vivo. *Nature* **475**, 501–505 (2011). doi: 10.1038/nature10193; pmid: 21706031
70. Z. Varga, H. Jia, B. Sakmann, A. Konnerth, Dendritic coding of multiple sensory inputs in single cortical neurons in vivo. *Proc. Natl. Acad. Sci. U.S.A.* **108**, 15420–15425 (2011). doi: 10.1073/pnas.1112355108; pmid: 21876170
71. M. E. Sheffield, D. A. Dombeck, The binding solution? *Nat. Neurosci.* **18**, 1060–1062 (2015). doi: 10.1038/nn.4075; pmid: 26216459
72. J. Courchet *et al*., Terminal axon branching is regulated by the LKB1-NUAK1 kinase pathway via presynaptic mitochondrial capture. *Cell* **153**, 1510–1525 (2013). doi: 10.1016/j.cell.2013.05.021; pmid: 23791179
73. Data and code for: J. K. O'Hare, K. C. Gonzalez, S. A. Herrlinger, Y. Hirabayashi, V. L. Hewitt, H. Blockus, M. Szoboszlay, S. V. Rolotti, T. C. Geiller, A. Negrean, V. Chelur, F. Polleux, A. Losonczy, Compartment-specific tuning of dendritic feature selectivity by intracellular Ca^{2+} release, Zenodo (2022); doi: 10.5281/zenodo.6051319

ACKNOWLEDGMENTS

We thank S. Fusi for productive discussion regarding intradendritic dynamics, T. Tabachnik and Zuckerman Institute Advanced Instrumentation for design of a custom-threaded optics adapter used to target virally labeled cells for electrophysiological recordings, A. Villegas for assistance piloting an immunoassay to validate the conditional knockout strategy, and A. Nelson and M. Rossi for invaluable comments on the manuscript. **Funding:** This work was supported by the National Institutes of Health (grants R01MH100631, R01NS094668, and U19NS104590 to A.L.; grants R01NS067557 and R01NS094668 to F.P.; grant F32MH118716 to J.K.O.; grant K00NS105187 to S.A.H.; grant F31MH117892 to S.V.R.; grant K99NS115984 to H.B.; and grant T32NS064928 to K.C.G.); the Japan Science and Technology Agency (JST PRESTO grant JPMJPR16F7 to Y.H.); the Zegar Family Foundation (A.L.); and the Foundation Roger De Spoelberch (F.P.). **Author contributions:** Conceptualization: J.K.O., A.L., F.P.; Data curation: J.K.O., K.C.G., S.V.R., V.C.; Formal analysis: J.K.O., V.L.H.; Funding acquisition: J.K.O., A.L., F.P.; Investigation: J.K.O., K.C.G., S.A.H., V.L.H.; Methodology: J.K.O., K.C.G., S.A.H., S.V.R., H.B., M.S., T.C.G., A.N., V.L.H., V.C.; Project administration: A.L., F.P.; Resources: Y.H., S.A.H., H.B., M.S., K.C.G., A.L., F.P.; Software: J.K.O., S.V.R., V.C., T.C.G.; Supervision: A.L., F.P.; Validation: J.K.O., S.A.H., K.C.G., V.L.H., V.C.; Visualization: J.K.O., S.A.H., Y.H., V.L.H.; Writing – original draft: J.K.O., A.L., F.P.; Writing – review and editing: all authors. **Competing interests:** The authors declare no competing interests. **Data and materials availability:** All plasmid DNA constructs generated in the course of this study are publicly available at Addgene. *Pdzd8*$^{F/F}$ mice are available upon request for academic, noncommercial use. Data and code are available at Zenodo (*73*).

SUPPLEMENTARY MATERIALS

science.org/doi/10.1126/science.abm1670
Materials and Methods
Figs. S1 to S15
Table S1
References (*74*–*89*)
Movie S1
MDAR Reproducibility Checklist

View/request a protocol for this paper from *Bio-protocol*.

30 August 2021; accepted 14 February 2022
10.1126/science.abm1670